Marginally-Stable Thermal Equilibria of Rayleigh-Bénard Convection

Liam O'Connor[1], Daniel Lecoanet[1,2], and Evan H. Anders[2]

[1]*Department of Engineering Sciences and Applied Mathematics,*
Northwestern University, Evanston, IL 60208 USA and
[2]*Center for Interdisciplinary Exploration and Research in Astrophysics,*
Northwestern University, Evanston, IL, 60201 USA

Natural convection is ubiquitous throughout the physical sciences and engineering, yet many of its important properties remain elusive—particularly in the large Rayleigh number regime. In this investigation, we derive and solve a quasilinear form of the Rayleigh-Bénard problem by representing the perturbations in terms of marginally stable eigenmodes. The amplitude of each eigenmode is determined by requiring that the background state maintains marginal stability. The background temperature profile evolves due to the advective flux of each eigenmode, as well as diffusion. The entire calculation is one-dimensional, and can be run on a workstation. We find the background temperature field evolves to an equilibrium state, where the advective flux from the marginally-stable eigenmodes and the diffusive flux sum to a constant. These marginally-stable thermal equilibria are exact solutions of the quasilinear equations. The mean temperature profile has thinner boundary layers and larger Nusselt numbers than thermally-equilibrated 2D and 3D simulations of the full nonlinear equations. We find the Nusselt number scales like $\mathrm{Nu} \sim \mathrm{Ra}^{1/3}$. When initializing a 2D simulation with a marginally-stable thermal equilibrium, we find the simulation does not exhibit the initial burst of turbulence typical of simulations initialized with the conductive background state plus noise. Although the Nu quickly equilibrates in these simulations, the kinetic energy evolves on a viscous timescale as domain-filling flywheel flows viscously attenuate.

I. INTRODUCTION

Rayleigh-Bénard convection plays a foundational role in astrophysical and geophysical settings. The resulting buoyancy-driven flows regulate heat transfer and generate large-scale vortices [1]. Turbulent convection, which is associated with large Rayleigh numbers Ra, is difficult to simulate. State of the art simulations performed by [2] have reached $\mathrm{Ra} \sim 10^{14}$ but estimates for the sun's convective zone and earth's interior are $\mathrm{Ra} \sim 10^{16}-10^{20}$ and $\mathrm{Ra} \sim 10^{20} - 10^{30}$ respectively [3, 4]. The scaling behavior of the Nusselt number $\mathrm{Nu} \sim \mathrm{Ra}^{\beta}$ in the asymptotic ultimate regime is of particular interest. There exists a substantial body of work pertaining to this specific topic with no general consensus [5–11].

Absent solid evidence from direct numerical simulation, other methods have been developed to try to infer large-Ra behavior or otherwise gain insight. In the presence of other physical effects (e.g., rotation, magnetic fields), one can sometimes derive an asymptotically consistent set of reduced equations [12, 13]. Reduced models are potentially useful in this context because they may allow us to study the problem with less expensive computations. Another approach relates to unstable exact coherent states (ECS) [14–17]. Simulations and analysis performed by [18, 19] suggest that chaotic solution trajectories might "visit" these ECS. Should that be the case, it is crucial that we discover and classify such equilibria.

Others have turned to studying quasilinear systems. The quasilinear approximation starts with a decomposition of all variables into a background and perturbations about this background. The approximation is to neglect the influence of nonlinear interactions between the perturbations on the perturbations themselves [20]. This renders the perturbation equations linear. Although the quasilinear approximation greatly simplifies the problem, an additional condition must be imposed to determine the amplitude of the perturbations. In [21], researchers compute ECS in parallel shear flows by deriving and solving a quasilinear formulation of the Navier-Stokes equations via multi-scale asymptotic arguments. They assume the background velocity evolves on a slow timescale, and to determine the perturbation amplitudes they require marginal stability at each timestep. A similar strategy is employed by [22] to studying acoustic streaming. In that work, an analytic expression for the first-order perturbation's amplitude is found by deriving a solvability condition.

In this paper we solve the Rayleigh-Bénard convection problem using an analogous strategy. In section II we recall the underlying equations, and in section III we describe how we evolve the background temperature profile while maintaining marginal stability. Section IV describes the properties of the marginally-stable thermal equilibria, in particular how the Nusselt number and characteristic wavenumbers vary with the Rayleigh number. Finally, we describe the results of simulations initialized with marginally-stable thermal equilibria in section V, and conclude in section VI.

II. MODEL SETUP

We begin with the Boussinesq approximation for Rayleigh-Bénard Convection, nondimensionalized on the freefall timescale. The domain $\mathcal{D}$ is 2-dimensional, rectangular, and horizontally periodic with spatial dimensions $0 < x < 4$ and $-1/2 < z < 1/2$. The fluid of

interest is constrained between two flat boundaries at $z = -1/2$ and $z = 1/2$ with fixed temperatures $1/2$ and $-1/2$ respectively. At both boundaries we specify impenetrable, no-slip conditions, such that the velocity $\boldsymbol{u} = u\hat{x} + w\hat{z} = \boldsymbol{0}$ at $z = \pm 1/2$, where $\hat{x}, \hat{z}$ are the unit vectors in the x and z directions. The equations of motion are then given by

$$\nabla \cdot \boldsymbol{u} = 0 \tag{1}$$

$$\frac{\partial \boldsymbol{u}}{\partial t} + \boldsymbol{u} \cdot \nabla \boldsymbol{u} = -\nabla p + T\hat{z} + \mathcal{R}\nabla^2 \boldsymbol{u} \tag{2}$$

$$\frac{\partial T}{\partial t} + \boldsymbol{u} \cdot \nabla T = \mathcal{P}\nabla^2 T \tag{3}$$

where p is pressure and T is temperature. For completeness, we specify a final boundary condition $p = p_0$ at $z = \pm 1/2$. Any system of this form can be characterized by its dimensionless Rayleigh number $\text{Ra} = \frac{g\alpha L^3 \Delta T}{\nu\kappa}$ and Prandtl number $\text{Pr} = \frac{\nu}{\kappa}$, where g, α, L, ΔT, ν, κ are the gravitational acceleration, coefficient of thermal expansion, domain height, opposed temperature difference, kinematic viscosity, and thermal diffusivity respectively. In this paper, we fix $\text{Pr} = 1$. For convenience, we define

$$\mathcal{R} = \sqrt{\frac{\text{Pr}}{\text{Ra}}}, \qquad \mathcal{P} = \frac{1}{\sqrt{\text{Pr}\,\text{Ra}}}. \tag{4}$$

To derive the quasilinear form, we posit that an arbitrary field f can be represented as the sum of a mean profile (denoted by $\bar{f}$) and a perturbation function (denoted by f').

$$\boldsymbol{u}(x, z, t) = \boldsymbol{u}'(x, z, t) \tag{5}$$

$$= u'(x, z, t)\hat{x} + w'(x, z, t)\hat{z} \tag{6}$$

$$T(x, z, t) = \bar{T}(z, t) + T'(x, z, t) \tag{7}$$

$$p(x, z, t) = \bar{p}(z, t) + p'(x, z, t). \tag{8}$$

where the mean-velocity components vanish due to incompressibility and symmetry. Perturbations are defined to have no horizontal-average

$$\langle f'(x, z, t)\rangle_x \equiv \int_0^4 f'(x, z, t)dx = 0. \tag{9}$$

Substituting (7) into (3) and taking the horizontal-average reduces the system to a simple initial value problem (IVP) for $\bar{T}$

$$\frac{\partial \bar{T}}{\partial t} + \frac{\partial}{\partial z}\langle w'T'\rangle_x = \mathcal{P}\frac{\partial^2 \bar{T}}{\partial z^2}, \tag{10}$$

with associated boundary conditions $\bar{T}(-1/2, t) = 1/2$ and $\bar{T}(1/2, t) = -1/2$. It should be noted that we could obtain a similar IVP for u by breaking symmetry and considering some nontrivial mean horizontal flow $\bar{u}(z, t)$. However we must have $\bar{w}(z, t) = 0$ due to incompressibility.

Substituting (8) into (2) and taking the horizontal average reveals that the mean pressure field $\bar{p}(z)$ must satisfy

$$0 = -\frac{\partial \bar{p}}{\partial z} + \bar{T} \tag{11}$$

To solve (10) numerically, we need an expression for the perturbation so we can calculate the advective heat flux. Here we will make the quasilinear approximation, dropping the $\boldsymbol{u}' \cdot \boldsymbol{\nabla} \boldsymbol{u}'$ and $\boldsymbol{u}' \cdot \boldsymbol{\nabla} T'$ terms from the evolution equations for the perturbations. Substituting (5)–(8) into (1)–(3) followed by subtracting (10) and (11) from the resulting temperature and $\hat{z}$ momentum equations gives

$$\nabla \cdot \boldsymbol{u}' = 0 \tag{12}$$

$$\frac{\partial \boldsymbol{u}'}{\partial t} = -\nabla p' + T'\hat{z} + \mathcal{R}\nabla^2 \boldsymbol{u}' \tag{13}$$

$$\frac{\partial T'}{\partial t} + \frac{\partial \bar{T}}{\partial z}w' = \mathcal{P}\nabla^2 T' \tag{14}$$

with Dirichlet boundary conditions

$$T'|_{z=\pm\frac{1}{2}} = 0, \quad u'|_{z=\pm\frac{1}{2}} = 0, \quad p'|_{z=\pm\frac{1}{2}} = 0. \tag{15}$$

This is now a linear problem in $\boldsymbol{u}'$ and T' which can be solved as an eigenvalue problem.

In his groundbreaking report [23], Lord Rayleigh observed that (12)–(14) can be manipulated into a separable form with generalized solutions

$$w'(x, z, t) = A\,\Re\left[W(z)\,e^{i(k_x x - st)}\right], \tag{16}$$

$$u'(x, z, t) = A\,\Re\left[U(z)\,e^{i(k_x x - st)}\right], \tag{17}$$

$$T'(x, z, t) = A\,\Re\left[\theta(z)\,e^{i(k_x x - st)}\right], \tag{18}$$

$$p'(x, z, t) = A\,\Re\left[P(z)\,e^{i(k_x x - st)}\right], \tag{19}$$

where A is the (undetermined) mode amplitude, $s = \omega + i\sigma$ and k_x is constrained, by periodicity, to the countably infinite set (spectrum) of wavenumbers

$$k_x \in \left\{\frac{n\pi}{2} \,\big|\, n \in \mathbb{N}\right\}. \tag{20}$$

We normalize the eigenmodes to have

$$\langle |\theta|^2\rangle_{\mathcal{D}} = 1 \tag{21}$$

where $\langle\cdot\rangle_{\mathcal{D}}$ denotes the spatial mean over the entire domain.

For each k_x, we can assess the stability of the perturbations by solving for the eigenvalue s, whose imaginary component σ plays the role of an exponential growth rate. Positive eigenvalues indicate that the system is unstable to small disturbances of wavenumber k_x, while negative eigenvalues indicate stability. A complete linear stability analysis requires solution over the full spectrum of

wavenumbers. The prototypical case is used to demonstrate that the critical Rayleigh number $\mathrm{Ra}_c = 1708$ when $\frac{\partial \bar{T}}{\partial z} = -1$.

To calculate the advective heat flux in equation 10, we can sum $\langle w'T' \rangle_x$ from each horizontal wavenumber individually. In this way, the heat flux from the perturbations influence the evolution of $\bar{T}$. But the evolution of $\bar{T}$ also influences the perturbations, as equation 14 depends on $\partial_z \bar{T}$. Thus, the mean temperature and perturbations fields are coupled.

III. PERTURBATION EVOLUTION

The linearized system (12)–(14) cannot determine the amplitude of the eigenmodes, A. However, the advective heat flux is proportional to A^2, so we need to specify the amplitude in order to solve equation 10. To evolve $\bar{T}$, we assume the perturbations evolve on a much faster timescale than the mean temperature, as in [22]. Stable modes ($\sigma < 0$) decay away rapidly. Unstable modes ($\sigma > 0$) will not persist on the slow timescale because the advective term $\langle w'T' \rangle_x$ tends to stabilize $\bar{T}$, thereby creating a negative feedback loop. Only marginally stable modes can be maintained on the slow timescale. Therefore the amplitude A must satisfy

$$\max_{k_x} \{\sigma\} = 0. \tag{22}$$

For various Ra and fixed Pr = 1, we seek marginally-stable thermal equilibria (MSTE) satisfying $\frac{\partial \bar{T}}{\partial t} = 0$ according to (10). We employ the `Dedalus` pseudo-spectral python framework [24] to solve the EVP outlined in Section II as well as the IVP (10) by representing each field with Chebyshev polynomials. We use the 3/2 dealiasing rule to calculate the advective heat flux. The necessary number of basis functions varies, as eigenfunctions and temperature profiles associated with large Ra admit increasingly small-scale features. A two-stage Runge-Kutta timestepper is implemented for the IVP. We use the `Eigentools` package [25] to manipulate the eigenfunctions and calculate the advective heat flux $\langle w'T' \rangle_x$.

At $t = 0$, we begin with a marginally-stable initial profile $\bar{T}(z, 0)$ whose construction is outlined in appendix A. At some arbitrary time $t = t_0 \geq 0$, we seek to evolve $\bar{T}(z, t_0)$ into a new marginally-stable profile $\bar{T}(z, t_0 + \Delta t)$ according to (10), using backward Euler to evolve the diffusion term and forward Euler to evolve the advection term. This requires us to determine the amplitude of the eigenfunction A. We will now illustrate our method of finding A^2 through an example.

An iteration is performed as follows. Consider a marginally-stable temperature profile $\bar{T}(z, t_0)$. By definition, its maximum eigenvalue is 0. Diffusing $\bar{T}(z, t_0)$ tends to increase its eigenvalues. Ignoring the diffusive term and evolving according to advection tends the stabilize the system. The appropriate amplitude A^2 can then
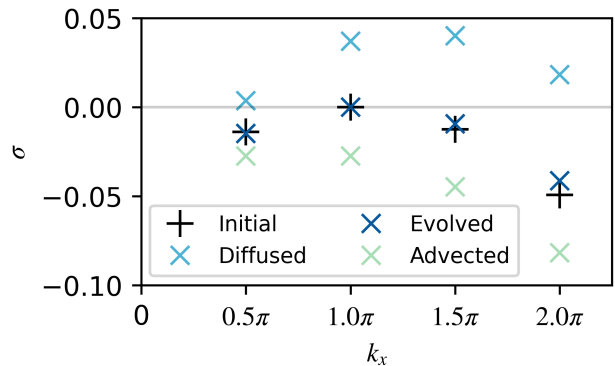

FIG. 1. Eigenvalue spectra for $\mathrm{Ra} = 10^5$. The spectrum of an "initial" marginally-stable mean temperature profile $\bar{T}(z, t_0)$ has a maximum eigenvalue of 0. Given a small fixed timestep Δt, diffusion destabilizes the system, increasing its eigenvalues. Advection tends to stabilize the system, decreasing its eigenvalues. We find the eigenfunction amplitude A^2 such that the combination of diffusion and advection yields a new, "evolved," marginally-stable mean temperature profile $\bar{T}(z, t_0 + \Delta t)$.

be approximated by

$$A^2 \approx -\frac{\sigma_{\mathrm{diff}}}{\sigma_{\mathrm{adv}}} \tag{23}$$

where σ_{diff} and σ_{adv} refer to the diffused and advected eigenvalues of the initially marginal mode. We illustrate these trends in Figure 1. $\bar{T}(z, t)$ is then evolved according to (10) and another eigenvalue solve is performed. Given a fixed timestep Δt, we assume the dominant eigenvalue can be described by a continuous function $\sigma_{\max}(A^2)$ which is locally differentiable. We use Newton's method to find an amplitude which satisfies our marginal stability tolerance criterion $|\sigma_{\max}(A^2)| < 10^{-9}$. Marginally-stable modes do not oscillate in time, i.e. $\sigma = 0$ implies $\omega = 0$. This agrees with the conventional notion of exchange of stabilities [26]. Crucially, we do not assume the k_x of the marginally-stable mode is fixed. In section III A we specify procedures for the treatment of multiple simultaneously marginal modes.

A. Treatment of multiple marginally-stable modes

In most cases, we encounter eigenvalue spectra with multiple simultaneously marginal modes. If ignored, we are forced to reduce the timestep and allow the modes to alternate which is marginally stable. Instead, we generalize the advective term in (10) to accommodate N simultaneously marginal modes

$$\langle w'T' \rangle_x = \sum_{n=1}^{N} 4A_n^2 \int \Re[W_n \theta_n^*] \, dz \tag{24}$$

where W_n and θ_n are the eigenmodes associated with $k_x = \frac{n\pi}{2}$. There are now N amplitudes to solve for and

N eigenvalues to keep marginally-stable. Given a small fixed time step Δt, let $\boldsymbol{A^2}$ be the amplitude vector and $\boldsymbol{\sigma}(\boldsymbol{A^2})$ be the dependent eigenvalues. We expect a function $\boldsymbol{\sigma} : \mathbb{R}^N \to \mathbb{R}^N$ to have isolated roots $\boldsymbol{\tilde{A}^2}$ (should they exist). A coarse approximation $\boldsymbol{A_0^2}$ for the appropriate amplitude vector $\boldsymbol{\tilde{A}^2}$ is given by a generalized form of (23):

$$\boldsymbol{\tilde{A}^2} \approx \boldsymbol{A_0^2} = -\Sigma_{\text{adv}}^{-1} \boldsymbol{\sigma_{\text{diff}}}. \tag{25}$$

Here $\boldsymbol{\sigma_{\text{diff}}} = \boldsymbol{\sigma}(\boldsymbol{0})$ refers to the eigenvalues after a brief Δt period of diffusion. $\Sigma_{\text{adv}} \in \mathbb{R}^{N \times N}$ is the matrix of eigenvalues after N periods of advection (one for each mode). In this way, an arbitrary element of Σ_{adv} represents how a particular mode's eigenvalue responds to the advection of another mode. At the point of our coarse estimate $\boldsymbol{A_0^2}$, we approximate the Jacobian matrix

$$J = \begin{bmatrix} \nabla\sigma_1(A_1, A_2, ..., A_N) \\ \nabla\sigma_2(A_1, A_2, ..., A_N) \\ \vdots \\ \nabla\sigma_N(A_1, A_2, ..., A_N) \end{bmatrix} \tag{26}$$

via first-order finite differences, requiring N^2 more individual EVP solves. A refined estimate is then given by

$$\boldsymbol{\tilde{A}^2} \approx \boldsymbol{A_1^2} = -J^{-1}\boldsymbol{\sigma}(\boldsymbol{A_0^2}). \tag{27}$$

Once constructed, we use each subsequent guess to adjust the Jacobian via Broyden's method for root-finding in multi-dimensional functions [27]. We find $\boldsymbol{\sigma}(\boldsymbol{A^2})$ does indeed have a unique root provided the time step is not too large and there are no numerical instabilities, as outlined in appendix **??**. Presumably this is due to the coupling of $\langle w'T'\rangle_x$ with $\bar{T}$. Over the course of a large time step, $\bar{T}$ evolves according to (10) and eventually the original eigenfunctions cease to provide a stabilizing influence.

Difficulty arises when transitioning between different numbers of marginal modes, particularly when stable modes become marginally-stable mid-iteration. We facilitate these transitions by defining an adjustable candidate tolerance $\varepsilon_{\text{cand}} \in [10^{-6}, 10^{-8}]$. We rely on $A^2 > 0$ by asserting that a mode which meets the candidate tolerance can be included as a candidate marginal mode. If the candidate mode's amplitude turns out to be positive, the candidate mode is now marginally-stable and can be regularly included in the subsequent iteration. If however we converge on a negative amplitude, the candidate mode must be discarded and the iteration is repeated.

After several time steps, $\bar{T}$ tends to asymmetrize due to numerical noise. Though asymmetric pairs of solutions may exist, we further constrain $\bar{T}$ by setting the coefficients of its even Chebyshev basis functions to zero at the start of each iteration.
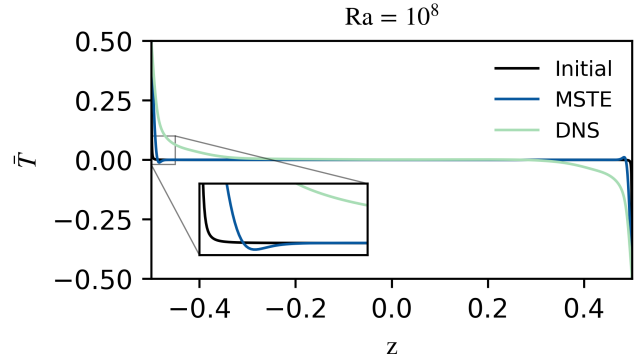

FIG. 2. Mean temperature profiles $\bar{T}$ for Ra $= 10^8$. The initial profile is given by (A1). We evolve this background temperature profile according to section III until we reach a marginally-stable thermal equilibrium (MSTE). The DNS curve is obtained from a 2D nonlinear simulation of (1)–(3) with `Dedalus`. DNS temperature data are horizontally- and time-averaged. The initial profile has the narrowest boundary layer, while the DNS profile has the widest boundary layer. The MSTE profile exhibits prominent dips, nested alongside the boundary regions.

IV. PROPERTIES OF THERMALLY EQUILIBRATED STATES

We evolve $\bar{T}$ as described above until $\max\{|\partial_t \bar{T}|\} < 10^{-5}$. In this marginally-stable thermal equilibrium, $\bar{T}$ does not evolve in time, and the perturbations also do not evolve in time, as they are marginally stable. Thus, these configurations are exact solutions to the quasilinear equations (equations 10–14). They differ from the usual ECS in that ECS are fixed points of the full nonlinear problem (1)–(3). Such definitions are not mutually exclusive, but in general we can assume that MSTE and ECS are not steady with respect to their counterparts' equations. We compute symmetric MSTE for Ra in the range $10^5 - 10^9$.

Figure 2 gives temperature profiles for Ra $= 10^8$ where the initial profile, whose construction is outlined in appendix A, is employed at iteration 0. Direct numerical simulations (DNS) are performed by solving (1)–(3) with `Dedalus`, followed by horizontal- and time- averaging. The DNS curve is more diffuse than the MSTE curve, which in turn, is more diffuse than the initial curve. Performing an eigenvalue solve by setting $\bar{T}$ equal to the DNS profile yields unstable eigenvalues. This suggests that MSTE might maximize boundary layer thickness, subject to the marginal stability constraint.

The most resilient and unexpected feature of MSTE temperature profiles are the pronounced dips adjacent to the boundary layers. These dips appear in every solution, regardless of Ra. Physically, they correspond to thin layers in which the mean temperature gradient reverses, contradicting an important hypothesis of [5, 6]. This counter-diffusion, which opposes overall heat trans-
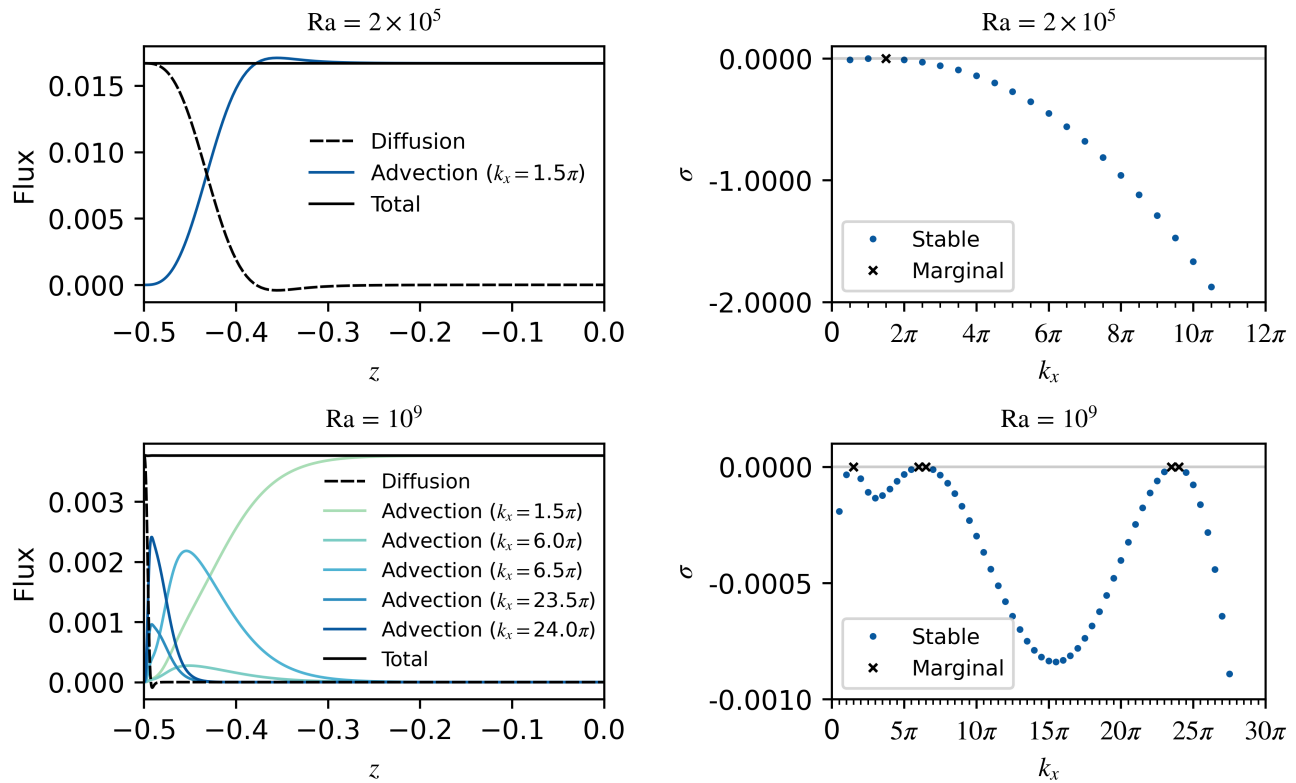
FIG. 3. Heat fluxes (left) and eigenvalue spectra (right) of equilibrated states Ra $= 2 \times 10^5$ (top) and Ra $= 10^9$ (bottom). The heat flux profiles are symmetric about $z = 0$, so we only plot for $z < 0$. Advection profiles belong to marginally-stable modes. For low Ra, a single mode with $k_x = 1.5\pi$ is sufficient to oppose boundary layer diffusion and facilitate heat flux throughout the bulk of the domain. For large Ra, high-wavenumber modes contribute pronounced small-scale advection profiles which tightly hug the thin boundary layers. A combination of of progressively wider advection profiles is necessary to transition to the $k_x = 1.5\pi$ mode.

fer, is overcome by the coinciding advective flux, shown in Figure 3. We do not understand the source of these dips, but similar temperature gradient reversals were reported by [17] along the midlines of 2D convective cellular solutions at Ra $\sim 10^6$. In that case, the reversals were due to nonlinear advection, which is not present in our quasilinear model.

In Figure 3, where we give heat flux profiles and eigenvalue spectra for two cases: Ra $= 2 \times 10^5$ (top) and Ra $= 10^9$ (bottom). For Ra $= 2 \times 10^5$, there is a single marginal mode at $k_x = 1.5\pi$ whose advective flux occupies the bulk of the domain. These states have wide boundary layers which gradually subside as advection becomes the dominant flux component. Transitional regions occur over a smaller length scale for Ra $= 10^9$ where the shift from diffusion to advection is sharp. At Ra $= 10^9$ we find five marginally-stable modes are necessary to reach an MSTE. Thin advection profiles, belonging to high-wavenumber modes with $k_x = 23.5\pi, 24\pi$, hug the boundary layer. Closer to the bulk of the domain, we see wider advection profiles corresponding to modes in a second group of marginal modes $k_x = 6\pi, 6.5\pi$. The $k_x = 1.5\pi$ mode forms the large-scale convective cell

structures observed in DNS, again occupying the bulk of the domain. The pairs of modes $k_x = 6\pi, 6.5\pi$ and $k_x = 23.5\pi, 24\pi$ are each associated with a single maximum in our plots of growth rate σ as a function of k_x (lower right panel of Figure 3). If we allowed wavenumbers to vary continuously, there would be an unstable mode between these pairs of wavenumbers. However, since we have fixed the horizontal size of our domain, we are left with pairs of discrete margin modes.

MSTE for large Ra tend to have a diverse combination of marginal modes. In every case, the $k_x = 1.5\pi$ mode is included. In Figure 4 we give the wavenumbers k_x of marginal modes. Sometimes we find two marginally-stable modes with wavenumbers separated by $\pi/2$. Like $k_x = 6\pi, 6.5\pi$ and $k_x = 23.5\pi, 24\pi$ for the Ra $= 10^9$ MSTE, these are due to the discretization of wavenumbers from our domain of width 4. We think of the pairs of modes as acting together as part of a single maximum of the growth rate as a function of the wavenumber. When wavenumbers are adjacent, we plot them in the same color and denote the larger mode with an x and the smaller with a +. For Ra $\geq 10^6$, a second branch of marginal modes is shown in light green. Least-squares
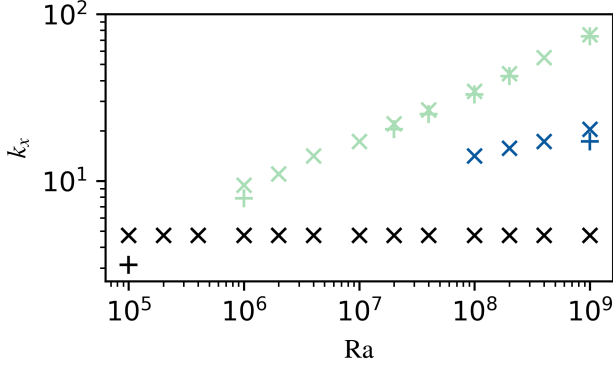
FIG. 4. Wavenumbers of marginally-stable modes in thermally equilibrated states. Marginal modes often appear in adjacent pairs, which we denote with a common color. For example, the spectrum corresponding to Ra = 10^5 has adjacent marginal wavenumbers $k_x = \pi$, 1.5π. The Ra = 10^9 spectrum, shown in lower right corner of Figure 3, has three groups of maxima, with a single marginal mode in the first group ($k_x = 1.5\pi$), two adjacent marginal modes in the second group ($k_x = 6\pi$, 6.5π), and two adjacent marginal modes in the third group ($k_x = 23.5\pi$, 24π). The largest wavenumbers of the green branch obey a power-law relationship with Ra

FIG. 5. For Ra $\geq 10^6$, the maximum marginally-stable wavenumber (corresponding to the green x markers in Figure 4) are inversely related to the boundary layer height δ. $(\max\{k_x\})^{-1}$ gives a minimum x length scale for the perturbations, and consequently, the advection. For large Ra, the boundary layers admit small scale features, requiring more vertical basis functions (higher resolution). The boundary layer width gives an estimate of the minimum vertical lengthscale in the problem. This suggests that the minimum horizontal and vertical lengthscales are proportional to each other over a wide range of Ra.

regression gives $\max\{k_x\} \propto \text{Ra}^{0.300}$ with $R^2 = 0.998$ for this maximum branch. For large Ra, the advective fluxes of this maximum branch opposes the strong diffusion of the thin MSTE boundary layers. At Ra $\geq 10^8$, a third branch appears (shown in blue), splitting the widening gap between the other two. For these points regression gives $k_x \propto \text{Ra}^{0.155}$ with $R^2 = 0.988$ This development is associated with moderately wide advection profiles, filling a niche in the total flux by uniting the thin profiles of the maximum branch with those of the bulk-domain-oriented minimum branch.

The largest marginal wavenumber $\max\{k_x\}$ (represented by the light green branch in Figure 4) serves as an inverse minimum length-scale in the x direction. The finest vertical structures in $\bar{T}(z)$ appear near the boundaries, requiring more basis functions (resolution) at large Ra. Naturally, this provides a complementary minimum length-scale for z. We define the boundary layer width δ as the distance from the boundary where $\partial_z T$ equals zero, i.e.,

$$\frac{\partial \bar{T}}{\partial z}\bigg|_{z=-\frac{1}{2}+\delta} = 0. \tag{28}$$

This height corresponds to the local extrema of the MSTE temperature profile, e.g., in Figure 2. In Figure 5, we show $\max\{k_x\}$ is proportional to δ over our range of Ra. Least-squares regression gives $\delta^{-1} = 1.71 \max\{k_x\} - 2.13$ with $R^2 = 0.996$. We can assume from this length scale agreement that the mean-squared x and z components of the temperature and velocity gradients are pro-
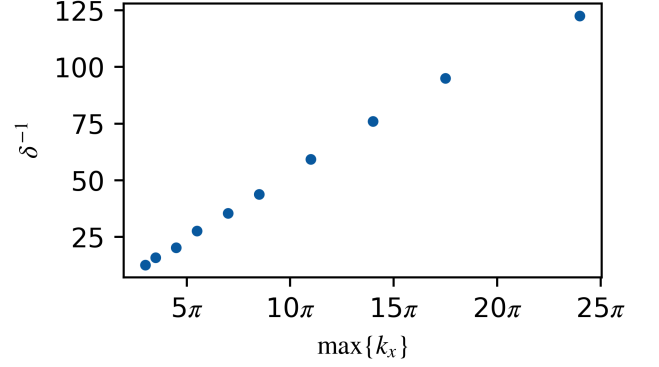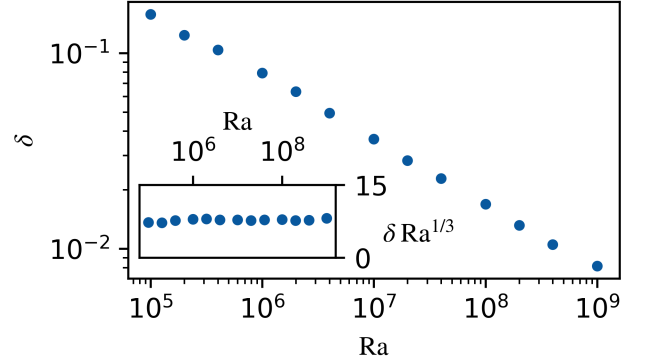

FIG. 6. Boundary layer height δ of MSTE. We define the boundary layer height based off the location where $\frac{\partial \bar{T}}{\partial z} = 0$ (see equation 28). Plotting on a log-log scale, we find that δ and Ra obey a power-law relationship. We also demonstrate that $\text{Ra}^{1/3}\delta$ is approximately constant with respect to Ra which is consistent with [5]

portional

$$\left\langle \frac{\partial T}{\partial x} \cdot \frac{\partial T}{\partial x} \right\rangle_{\mathcal{D}} \propto \left\langle \frac{\partial T}{\partial z} \cdot \frac{\partial T}{\partial z} \right\rangle_{\mathcal{D}}$$
$$\left\langle \frac{\partial \boldsymbol{u}}{\partial x} \cdot \frac{\partial \boldsymbol{u}}{\partial x} \right\rangle_{\mathcal{D}} \propto \left\langle \frac{\partial \boldsymbol{u}}{\partial z} \cdot \frac{\partial \boldsymbol{u}}{\partial z} \right\rangle_{\mathcal{D}}. \tag{29}$$

This is consistent with the mean squared gradient assumptions of [5].

We find the MSTE can be characterized by their boundary layer height. In Figure 6, we illustrate the scaling behavior of the boundary layer height $\delta =$

Ra$^{-1/3}$. This is consistent with Malkus' classical marginal-stability theory, a scaling argument which perceives the boundary regions as subdomains which are themselves marginally-stable [5].

The Nusselt number, which measures convective performance is given by

$$\text{Nu} = \frac{\langle \langle w'T' \rangle_x - \mathcal{P}\frac{\partial \bar{T}}{\partial z} \rangle_z}{\langle -\mathcal{P}\frac{\partial \bar{T}}{\partial z} \rangle_z}. \tag{30}$$

There is no general consensus surrounding the scaling behavior of Nu for high Ra systems, which are of particular importance in astrophysical and geophysical systems. In Figure 7 we report Nu for MSTE, "steady rolls" ECS [16], and DNS [28, 29]. We find that MSTE satisfy Nu $\sim$ Ra$^{1/3}$, consistent with our finding that the boundary layer width scales like $\delta \sim$ Ra$^{1/3}$. The Nusselt numbers of the ECS are somewhat lower and the DNS Nusselt numbers are yet lower still. In both cases, the Ra dependence appear slightly more shallow than for the MSTE. [16] hypothesized that the Nu of all ECS which admit classical Malkus scaling must always exceed the Nu of turbulent convection. If we generalize this notion to include quasilinear equilibria, our findings agree; MSTE have larger Nu than 2D and 3D DNS. This might be due to the chaotic transitions among the unstable periodic orbits outlined by [18, 19] inhibiting heat flux. We might also anticipate the existence of similar equilibria with smaller Nu, occupying complementary nodes in the Markov chain whose behavior agrees with DNS.

V. SIMULATIONS WITH THERMALLY EQUILIBRATED INITIAL CONDITIONS

This investigation is partially motivated by the prospect of decreasing DNS runtimes by employing MSTE as initial conditions. One common choice of initial conditions for DNS of equations (1)–(3) are

$$T(x,z)\big|_{t=0} = 0.5 - z + N$$
$$\boldsymbol{u}(x,z)\big|_{t=0} = \boldsymbol{0}$$
$$p(x,z)\big|_{t=0} = 0 \tag{31}$$

where N is low-amplitude random noise. Here we instead initialize using the MSTE,

$$T(x,z)\big|_{t=0} = \bar{T}(z) + \sum_{n=1}^{N} A_n \Re\Big[\theta_n(z) e^{ik_{x_n}x}\Big] + N$$

$$\boldsymbol{u}(x,z)\big|_{t=0} = \sum_{n=1}^{N} A_n \Re\Big[\Big(U_n(z)\hat{x} + W_n(z)\hat{z}\Big) e^{ik_{x_n}x}\Big]$$

$$p(x,z)\big|_{t=0} = \sum_{n=1}^{N} A_n \Re\Big[P_n(z) e^{ik_{x_n}x}\Big] \tag{32}$$

where $\theta_n(z), U_n(z), W_n(z), P_n(z)$; A_n; and k_{x_n} refer to the complex eigenfunctions, amplitude, and wavenumber

at the nth marginal mode respectively. Note that although the MSTE is an equilibrium of the quasilinear equations, it is not an equilibrium of the full nonlinear equations. Accordingly the simulation state would evolve on initialization absent a random noise term. Here we include noise as a source of asymmetries.

Simulations initialized with the conductive equilibrium plus low-amplitude thermal noise have a large peak in Nu early on in their evolution (Figure 8). This is due to a burst of turbulence which occurs when the convective motions first become nonlinear. A simulation initialized with the MSTE, however, does not exhibit this transient burst of turbulence, as the large-scale anatomy of convective cells exists on initialization. Simulation of this transitional period is prohibitive [30]. For high Ra experiments, researchers often "bootstrap" data by initializing simulations with the results of similar Ra runs [28, 31]. MSTE can be perceived as a set of initial conditions, designed for avoiding the simulation of transitional high Reynolds number flows.

MSTE are laminar, lacking the small-scale structures associated with moderate to high Ra experiments. This is an apparent consequence of the quasilinear assumptions. If we perceive MSTE as background states, DNS suggest that plumes, vortex sheets, and other unstable turbulent features inhibit total heat transfer. This perspective agrees with conventional models of transitions to turbulent flows, such as Boussinesq's turbulent-viscosity hypothesis [32]. The emergence of small-scale velocity structures tends to increase total shear [26, 33, 34], thereby impeding buoyancy-driven flows and decreasing advection in the bulk of the domain. We could also attribute the diffuse DNS temperature profile in Figure 2 with unsteady boundary-layer penetration and mixing that MSTE do not exhibit.

We also find that the average kinetic energies of simulations initialized with MSTE are significantly larger than those found in simulations initialized with the conductive state plus noise, as shown Figure 9. This is because the MSTE contain strong large-scale flows, which decay on a viscous time-scale

$$t_\nu \sim \sqrt{\frac{\text{Ra}}{\text{Pr}}}.$$

Consequently, MSTE initial conditions do not reduce the simulation time required to achieve a statistically-steady state—rather they increase it considerably! This suggests the MSTE background state perspective is partially flawed, as a more useful background state would approximate the kinetic energy with more fidelity.

VI. DISCUSSION

In this paper we describe a new way to study Rayleigh–Bénard convection. We compute marginally-stable thermal equilibria (MSTE), which are equilibria of the quasilinear equations. To compute MSTE, we
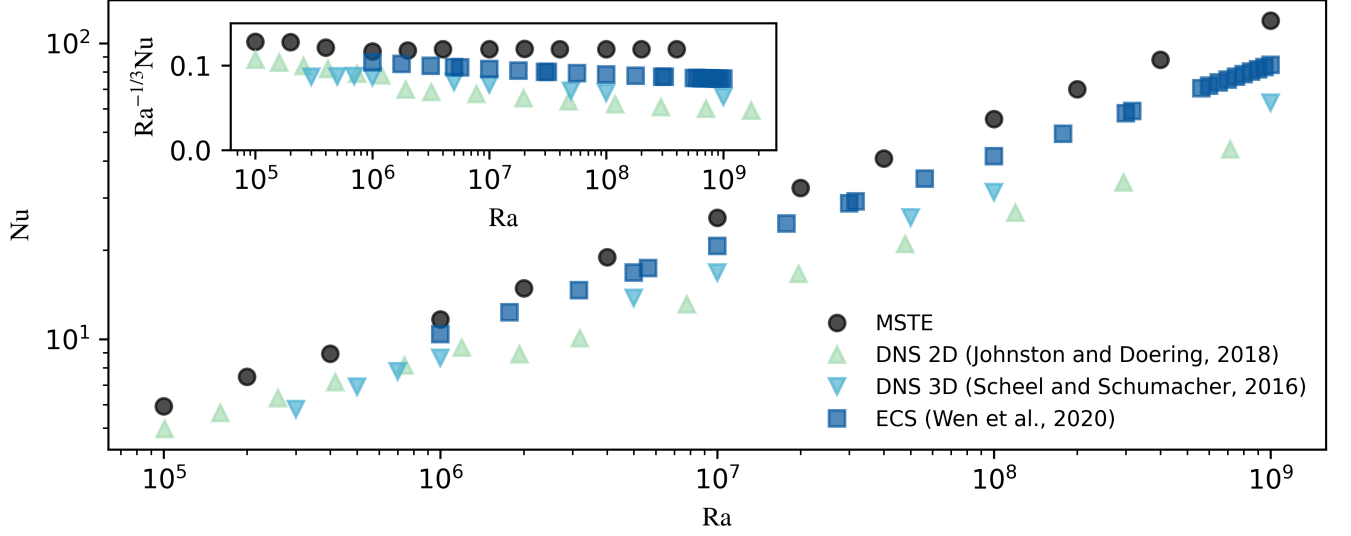
FIG. 7. Nusselt numbers are shown for MSTE, aspect-ratio-optimized "steady rolls" ECS [16], as well as statistically-steady 2D and 3D DNS [28, 29]. All datasets obey power-law relationships, with the MSTE and ECS scaling like $\mathrm{Nu} \sim \mathrm{Ra}^{1/3}$. MSTE have greater Nu than the ECS, which in turn, have greater Nu than the DNS. This can be explained by the contrasting boundary layer geometries shown in Figure 2.
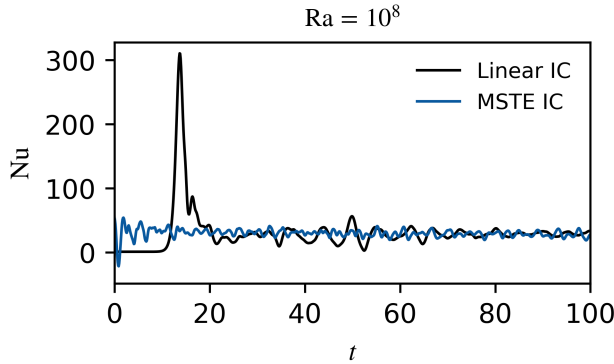

FIG. 8. Nusselt numbers of simulations performed at $\mathrm{Ra} = 10^8$, initialized with the conductive equilibrium plus thermal noise (black) and the MSTE (blue). MSTE simulations do not undergo a convective-transient period because the characteristic large-scale convective cell structure exists on initialization.

FIG. 9. Average kinetic energies are reported for the same simulations illustrated in Figure 8 ($\mathrm{Ra} = 10^8$). The eigenfunctions belonging to MSTE have significantly more kinetic energy than the statistically-steady state. Kinetic equilibrium is achieved on the viscous time-scale $t_\nu \sim \sqrt{\mathrm{Ra}/\mathrm{Pr}}$.

construct a marginally-stable mean temperature profile and evolved it according to the advective flux of its marginally-stable eigenfunctions, and its own diffusion. We assume that at least some modes are always in a marginally-stable configuration. The marginal stability constraint then fixes the ratio between advection and diffusion (eigenfunction amplitude A^2). We use standard root-finding algorithms to solve for the appropriate A^2 at each iteration, until, the fixed combination of diffusion and advection sum to a constant flux. The MSTE calculation is a one-dimensional problem, com-
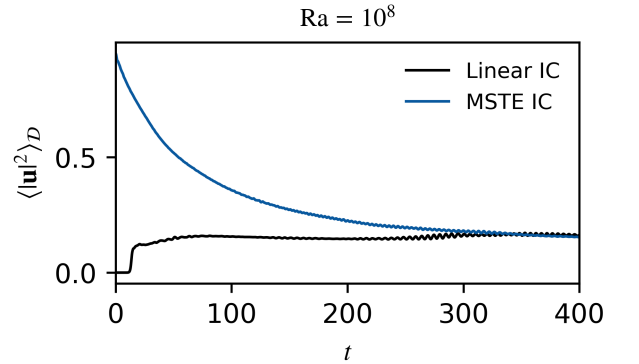
bining eigenvalue solves, and the time evolution of the one-dimensional mean temperature profile. Thus, they can be calculated on a single workstation.

The MSTE retain several key features that are prevalent in experiments and simulations: $\mathrm{Nu} \sim \mathrm{Ra}^{1/3}$ scaling, large-scale convective cell structures, and minimum length scale agreement. They also exhibit unique and unexpected features: mean temperature gradient-reversals/dips, high kinetic energy flows, and a larger Nu than other time-invariant solutions. When initializing with different mean temperature profiles, we found the same MSTE, suggesting these equilibria might be unique.

Simulations initialized with the MSTE (32) do not undergo an early convective transient period, but have faster flows when compared with DNS. From a dynamical systems perspective, unstable orbits depart from MSTE and approach the global attractor on a viscous time-scale. This requires more computational effort to achieve relaxation when compared to the conventional conductive initial condition (31).

As previously noted, using the mean temperature in a statistically-steady DNS as a background state for an eigenvalue problem yields positive eigenvalues: the system is in a perpetual state of instability. Unstable modes tend to stabilize the system rapidly, creating a negative feedback loop whose average state is linearly unstable. We might curtail the disagreement between MSTE and DNS by adjusting our marginal-stability criterion. Should the fast and slow time scales not be entirely separate, we might anticipate the long-term persistence of moderately unstable modes. To find MSTE, we initialize the time-evolution algorithm with the analytic temperature profile derived by [35]. This involves modifying the boundary layer thickness δ_0 to achieve marginal stability.

Instead of imposing marginal stability, we can use quasilinear model to thermally-equilibrate and expand 1D approximations into 2D. As previously noted, there is no shortage of theories pertaining to the scaling behavior Nu $\sim$ Ra$^\beta$ [5–11]. For large Ra, we can approximate $\delta_0 \approx$ Nu^{-1} and construct a 1D temperature profile according to (A1) or some other approximation. In this way, other 2D quasilinear thermal equilibria can be obtained and analyzed.

Appendix A: Initial buoyancy profile

We initialize the thermal-equilibration algorithm with [35]'s analytical thermal boundary layer equation for turbulent Rayleigh-Bénard convection, given by

$$\bar{T}_0(\xi) = \frac{\sqrt{3}}{4\pi} \log \frac{(1+a\xi)^3}{1+(a\xi)^3} + \frac{3}{2\pi} \arctan\left(\frac{4\pi}{9}\xi - \frac{1}{\sqrt{3}}\right) + \frac{1}{4}$$
$$\xi = \frac{z}{\delta_0}, \qquad a = \frac{2\pi}{3\sqrt{3}} \tag{A1}$$

where δ_0 is the boundary layer height. We expect that each Ra is associated with a unique δ_0 for which $\bar{T}_0(z)$ is marginally-stable. It should be noted that when experimenting with various initial profiles (tanh, erf, etc.), we obtain indistinguishable equilibrated states, implying that solutions may be unique. An example of (A1) is given by the blue curve in Figure 2.

Appendix B: MSTE Metrics

Ra	Pr	$k = 2\pi/\Gamma$	$N_x \times N_z$	Nu	Re
$10^{13/4}$	1	π	128×65	1.056590	1.617336
1.9×10^3	1	π	128×65	1.145807	2.682155
2×10^3	1	π	128×65	1.212037	3.317190
2.25×10^3	1	π	128×65	1.355410	4.550975
2.5×10^3	1	π	128×65	1.474455	5.537770
2.75×10^3	1	π	128×65	1.575599	6.391812
3×10^3	1	π	128×65	1.663162	7.159844
$10^{14/4}$	1	π	128×65	1.714193	7.624400
3.5×10^3	1	π	128×65	1.808754	8.526064
4×10^3	1	π	128×65	1.926775	9.740578
4.5×10^3	1	π	128×65	2.025985	10.85141
5×10^3	1	π	128×65	2.111714	11.88534
$10^{15/4}$	1	π	128×65	2.204811	13.09152
8×10^3	1	π	128×65	2.476330	17.05494
10^4	1	π	128×65	2.648664	20.07400
$10^{17/4}$	1	π	128×65	3.122843	29.50047
$10^{18/4}$	1	π	128×65	3.665041	42.29585
$10^{19/4}$	1	π	128×65	4.287042	59.56858
10^5	1	π	128×65	4.994322	82.84462
$10^{21/4}$	1	π	128×65	5.795869	114.2355
$10^{22/4}$	1	π	128×97	6.703915	156.5252
$10^{23/4}$	1	π	128×97	7.732236	213.4031
10^6	1	π	128×97	8.896615	289.7982

			$N_x \times N_z$		
$10^{25/4}$	1	π	256×97	10.21546	392.2837
$10^{26/4}$	1	π	256×129	11.71065	529.6372
$10^{27/4}$	1	π	256×129	13.40898	713.6005
10^{7}	1	π	512×129	15.34493	959.9367
1.35×10^{7}	1	π	512×129	16.46456	1119.932
1.5×10^{7}	1	π	512×129	16.87881	1182.172
1.6×10^{7}	1	π	512×193	17.13944	1222.005
1.65×10^{7}	1	π	512×193	17.26636	1241.484
1.7×10^{7}	1	π	512×193	17.39216	1260.709
1.736×10^{7}	1	π	512×193	17.48282	1274.414
1.76×10^{7}	1	π	512×193	17.54351	1283.493
$10^{29/4}$	1	π	512×193	17.58987	1290.377
1.786×10^{7}	1	π	512×193	17.60946	1293.277
1.8×10^{7}	1	π	512×193	17.64500	1298.522
1.85×10^{7}	1	π	512×193	17.77160	1317.122
1.9×10^{7}	1	π	512×193	17.89693	1335.501
1.95×10^{7}	1	π	512×193	18.02044	1353.657
2×10^{7}	1	π	512×193	18.14193	1371.593
2.4×10^{7}	1	π	512×193	19.04221	1507.890
2.8×10^{7}	1	π	512×193	19.83413	1633.418
$10^{30/4}$	1	π	512×193	20.47798	1739.647
4.5×10^{7}	1	π	512×193	22.44036	2087.182
$10^{31/4}$	1	π	512×193	23.76002	2340.822
10^{8}	1	π	768×257	27.50669	3144.931
$10^{33/4}$	1	π	768×257	31.81154	4220.616
2.15×10^{8}	1	π	768×257	33.36657	4649.541
$10^{34/4}$	1	π	768×257	36.75427	5658.648
4.64×10^{8}	1	π	896×321	40.44652	6875.704
$10^{35/4}$	1	π	896×321	42.42917	7580.057
10^{9}	1	π	1024×321	48.94284	10145.79
$10^{37/4}$	1	π	1024×321	56.42926	13571.10
2.15×10^{9}	1	π	1024×321	59.13988	14935.81
2.5×10^{9}	1	π	1024×321	61.38714	16116.94
$10^{38/4}$	1	π	1024×321	65.06338	18145.61
$10^{153/16}$	1	π	1024×321	67.42466	19511.79
4×10^{9}	1	π	1024×321	68.96487	20429.24
4.64×10^{9}	1	π	1024×321	71.58241	22019.93
$10^{39/4}$	1	π	1024×321	75.09725	24262.22
10^{10}	1	π	1024×321	86.68318	32430.06
$10^{41/4}$	1	π	1024×321	100.0909	43339.02
2×10^{10}	1	π	1024×321	103.0738	45995.60
2.15×10^{10}	1	π	1024×321	104.9517	47705.08

Table S1: Details for numerical solutions with Pr = 1 and $\Gamma = 2$. N_x and N_z represent the numbers of Fourier and Chebyshev modes, respectively.

[1] L.-A. Couston, D. Lecoanet, B. Favier, and M. Le Bars, Phys. Rev. Research **2**, 023143 (2020).
[2] X. Zhu, V. Mathai, R. J. Stevens, R. Verzicco, and D. Lohse, Physical Review Letters **120** (2018), 10.1103/physrevlett.120.144502.
[3] M. Ossendrijver, Astronomy & Astrophysics Reviews **11**, 287 (2003).
[4] D. Gubbins, Physics of the Earth and Planetary Interiors **128**, 3 (2001), dynamics and Magnetic Fields of the Earth's and Planetary Interiors.
[5] W. V. R. Malkus, Proceedings of the Royal Society of London. Series A, Mathematical and Physical Sciences **225**, 196 (1954).
[6] L. N. Howard, in *Applied Mechanics*, edited by H. Görtler (Springer Berlin Heidelberg, Berlin, Heidelberg, 1966) pp. 1109–1115.
[7] R. H. Kraichnan, Physics of Fluids **5**, 1374 (1962).
[8] E. A. Spiegel, Journal of Geophysical Research **67**, 3063 (1962).
[9] B. Castaing, G. Gunaratne, L. Kadanoff, A. Libchaber, and F. Heslot, Journal of Fluid Mechanics **204**, 1 (1989).

[10] S. Grossmann and D. Lohse, Journal of Fluid Mechanics **407**, 27–56 (2000).

[11] G. Ahlers, S. Grossmann, and D. Lohse, Rev. Mod. Phys. **81**, 503 (2009).

[12] K. Julien and E. Knobloch, Journal of Mathematical Physics **48**, 065405 (2007).

[13] K. Julien, E. Knobloch, A. M. Rubio, and G. M. Vasil, Phys. Rev. Lett. **109**, 254503 (2012).

[14] F. Waleffe, A. Boonkasame, and L. Smith, Physics of Fluids **27**, 051702 (2015).

[15] D. Sondak, L. M. Smith, and F. Waleffe, Journal of Fluid Mechanics **784**, 565 (2015), arXiv:1507.03151 [physics.flu-dyn].

[16] B. Wen, D. Goluskin, and C. Doering, (2020).

[17] G. P. Chini and S. Cox, Physics of Fluids **21**, 083603 (2009).

[18] G. Yalnız, B. Hof, and N. Burak Budanur, arXiv e-prints , arXiv:2007.02584 (2020), arXiv:2007.02584 [physics.flu-dyn].

[19] P. Cvitanović and J. Gibson, Physica Scripta **2010**, 014007 (2010).

[20] J. B. Marston, G. P. Chini, and S. M. Tobias, Phys. Rev. Lett. **116**, 214501 (2016), arXiv:1601.06720 [physics.flu-dyn].

[21] C. Beaume, G. P. Chini, K. Julien, and E. Knobloch, Physical Review E **91** (2015), 10.1103/physreve.91.043010.

[22] G. Michel and G. P. Chini, Journal of Fluid Mechanics **858**, 536–564 (2019).

[23] L. R. O. F.R.S., The London, Edinburgh, and Dublin Philosophical Magazine and Journal of Science **32**, 529 (1916).

[24] K. J. Burns, G. M. Vasil, J. S. Oishi, D. Lecoanet, and B. P. Brown, Physical Review Research **2**, 023068 (2020), arXiv:1905.10388 [astro-ph.IM].

[25] J. Oishi, K. Burns, S. Clark, E. Anders, B. Brown, G. Vasil, and D. Lecoanet, "Eigentools: Tools for studying linear eigenvalue problems," (2021), ascl:2101.017.

[26] P. G. Drazin and W. H. Reid, *Hydrodynamic Stability*, 2nd ed., Cambridge Mathematical Library (Cambridge University Press, 2004).

[27] C. Broyden, Mathematics of Computation **19**, 577 (1965).

[28] H. Johnston and C. R. Doering, Phys. Rev. Lett. **102**, 064501 (2009).

[29] J. D. Scheel and J. Schumacher, Journal of Fluid Mechanics **802**, 147–173 (2016).

[30] E. H. Anders, B. P. Brown, and J. S. Oishi, Phys. Rev. Fluids **3**, 083502 (2018).

[31] R. Verzicco and R. Camussi, Physics of Fluids **9**, 1287 (1997), https://doi.org/10.1063/1.869244.

[32] J. Boussinesq, (1877).

[33] D. Lecoanet, M. McCourt, E. Quataert, K. Burns, G. Vasil, J. Oishi, B. Brown, J. Stone, and R. O'Leary, Monthly Notices of the Royal Astronomical Society **455**, 4274 (2016), publisher Copyright: © 2015 The Authors.

[34] S. B. Pope, *Turbulent Flows* (Cambridge University Press, 2000).

[35] O. Shishkina, S. Horn, S. Wagner, and E. S. C. Ching, Phys. Rev. Lett. **114**, 114302 (2015).